

The role of quasi-plasticity in the extreme contact damage tolerance of the stomatopod dactyl club

Shahrouz Amini¹, Maryam Tadayon¹, Sridhar Idapalapati² and Ali Miserez^{1,3*}

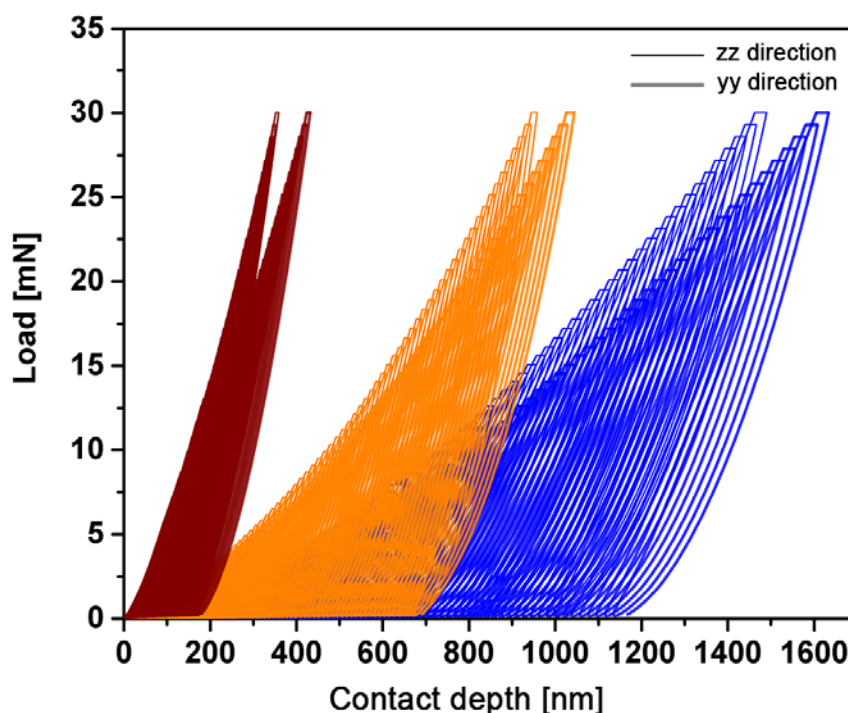
¹ School of Materials Science and Engineering, Nanyang Technological University, 50 Nanyang Avenue, Singapore 639798, Singapore.

² School of Mechanical & Aerospace Engineering, Nanyang Technological University, 50 Nanyang Avenue, Singapore 639798, Singapore.

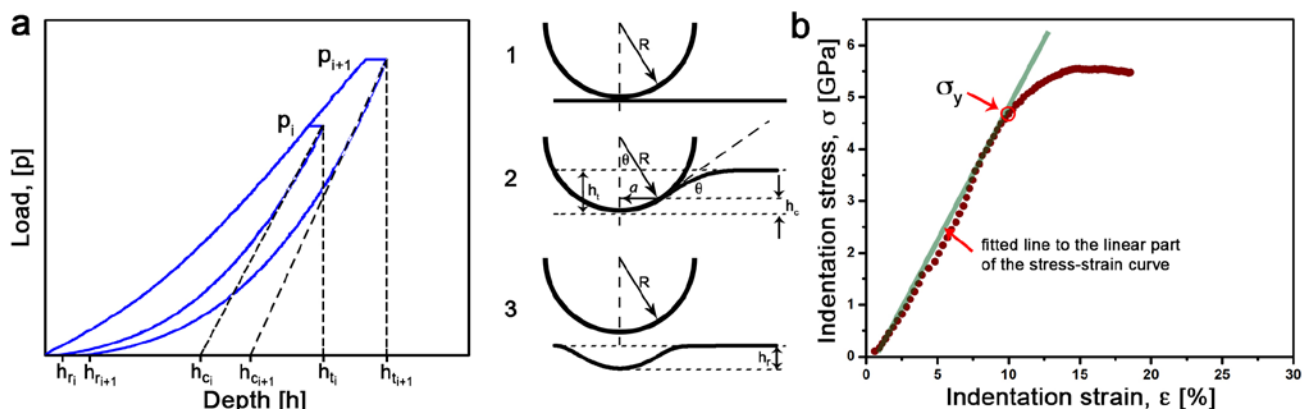
³ School of Biological Sciences, Nanyang Technological University, 60 Nanyang Drive, Singapore 637551, Singapore.

*Corresponding author: ali.miserez@ntu.edu.sg

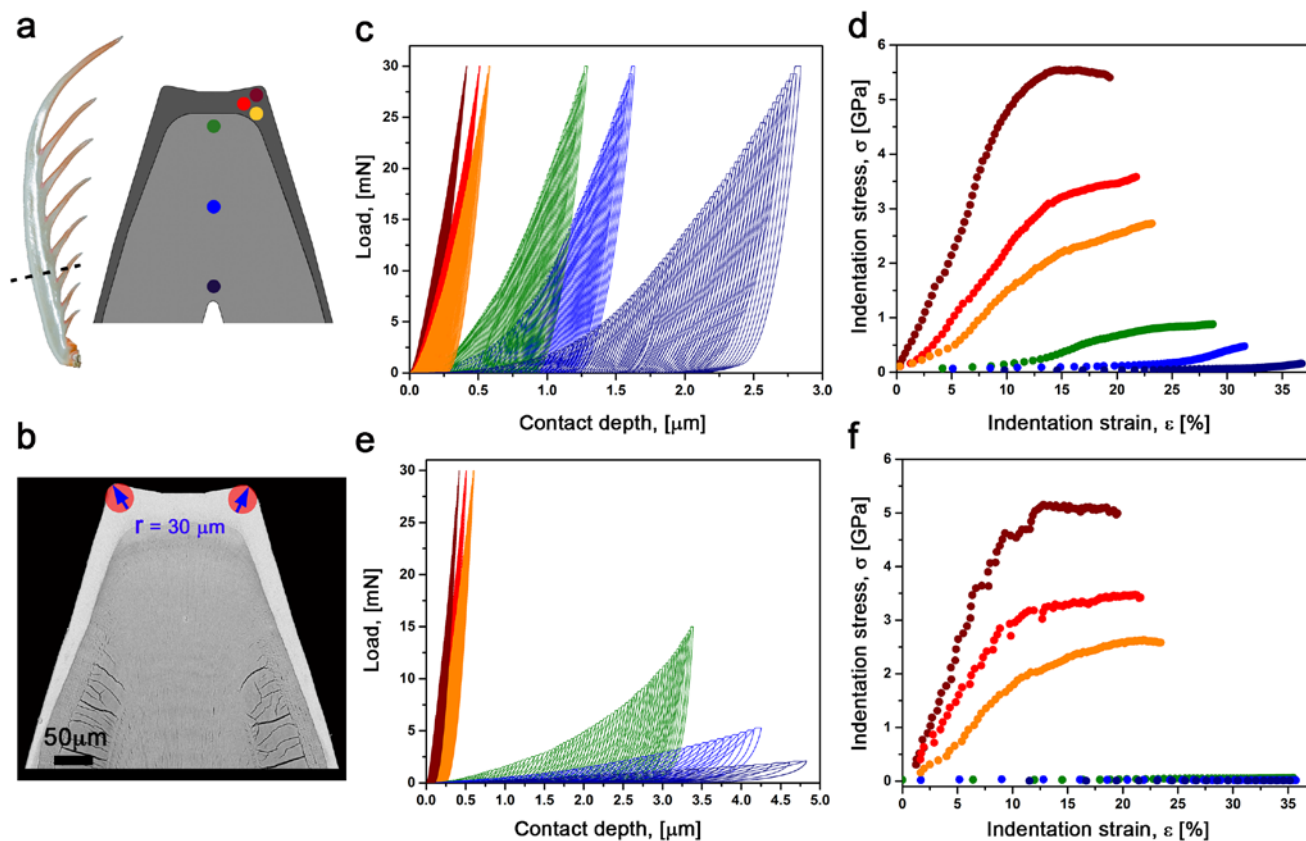
Supplementary Figures



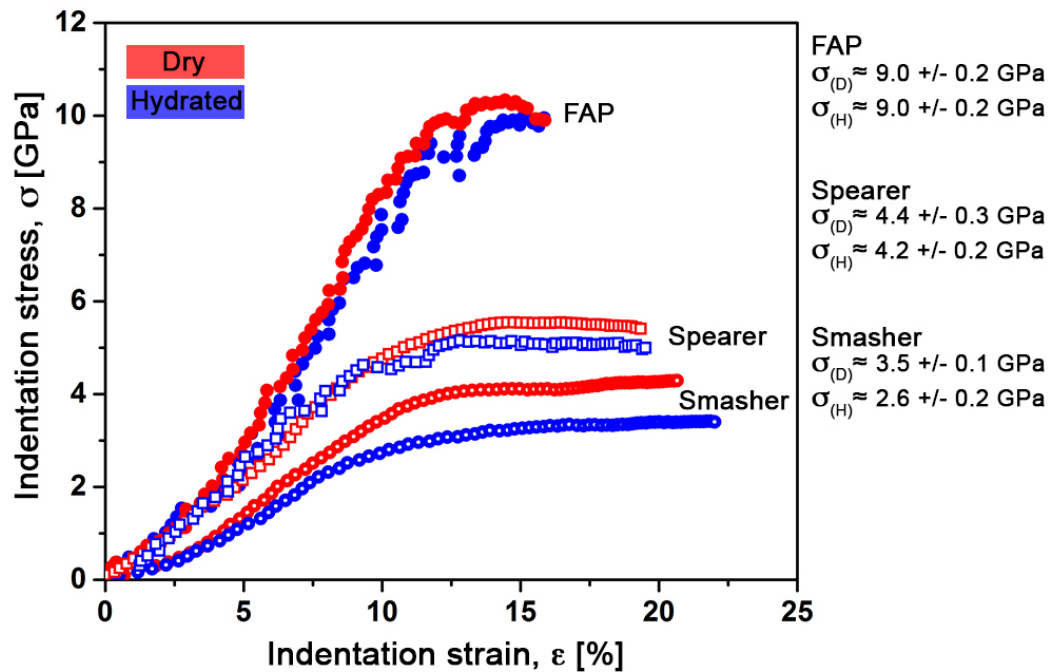
Supplementary Figure 1. Anisotropic response of the dactyl clubs as measured by partial loading-unloading curves in distinct layers. These curves were used to compute the indentation stress-strain curves shown in Figure 2d (same color coding as in the main text).



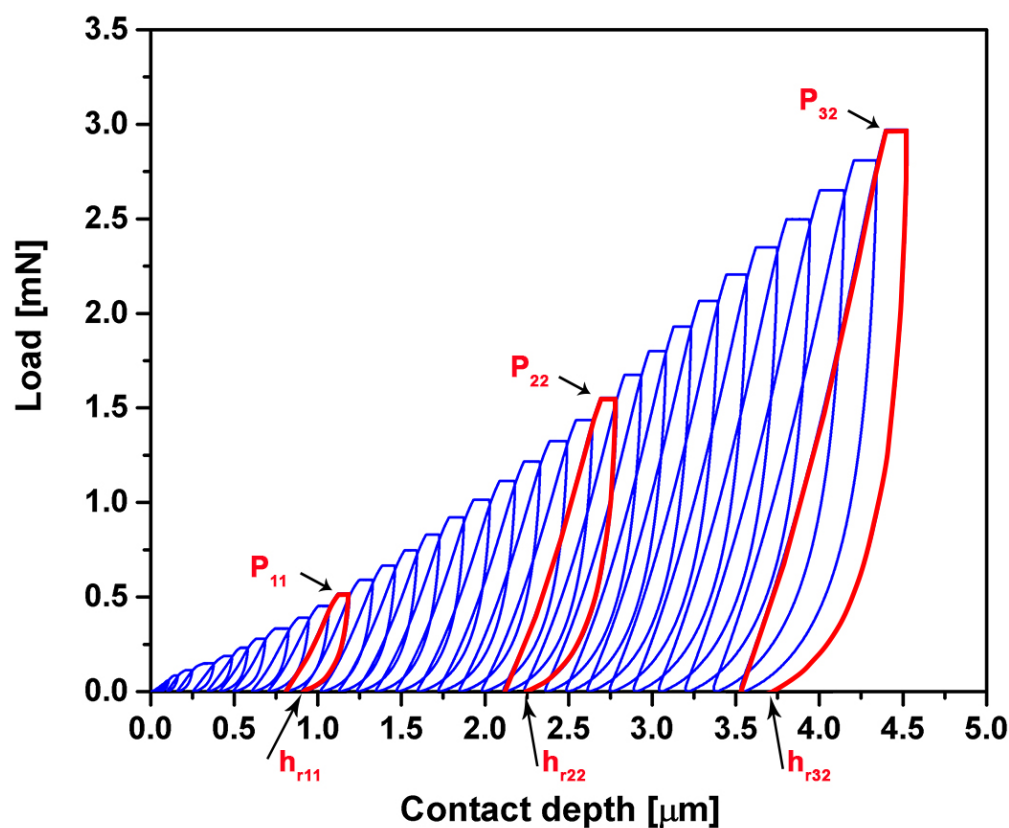
Supplementary Figure 2. Definition of the contact depth (h_c) and yield stress (σ_y) point of the indentation stress-strain curve. (a) Schematic of partial loading-unloading curves of two cycles (i and $i+1$), with definition of contact load (p_i), residual depth (h_{ri}), contact depth (h_{ci}), and maximum depth (h_{ti}). The contact depth (h_c) at each load was extracted to calculate the contact radius (a) and the mean contact pressure (P_m) (Supplementary Note 1). **(b)** Method used to identify the yield point. The initial linear portion of the stress-strain curve was obtained by curve fitting and the deviation with the indentation stress-strain curve represents the yield point.



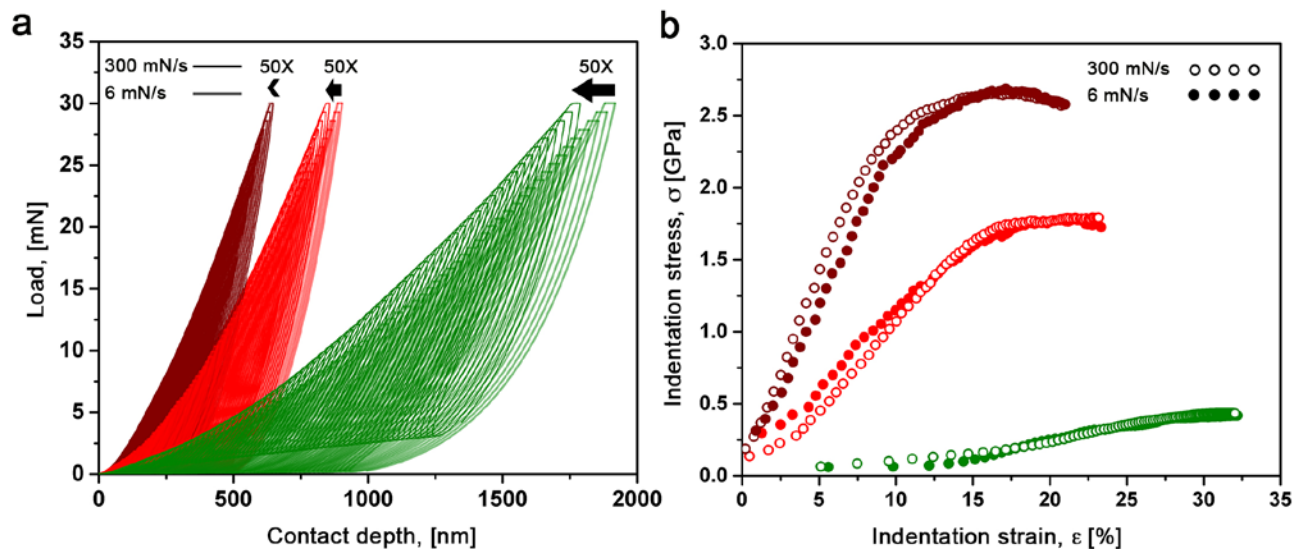
Supplementary Figure 3. Indentation response of the “spearer” mantis shrimp dactyl clubs for distinct layers. (a) Schematic cross section of a spearer sample, with color-coding representing the location where indentation measurements were carried out. (b) A low magnification FESEM image of a spear sample with its characteristic radius of curvature. (c) Partial loading-unloading curves for the dry spear sample. (d) Indentation stress-strain curves computed from the partial loading-unloading curves obtained in (c). (e,f) Partial loading-unloading curves and corresponding indentation stress-strain curves in hydrated conditions.



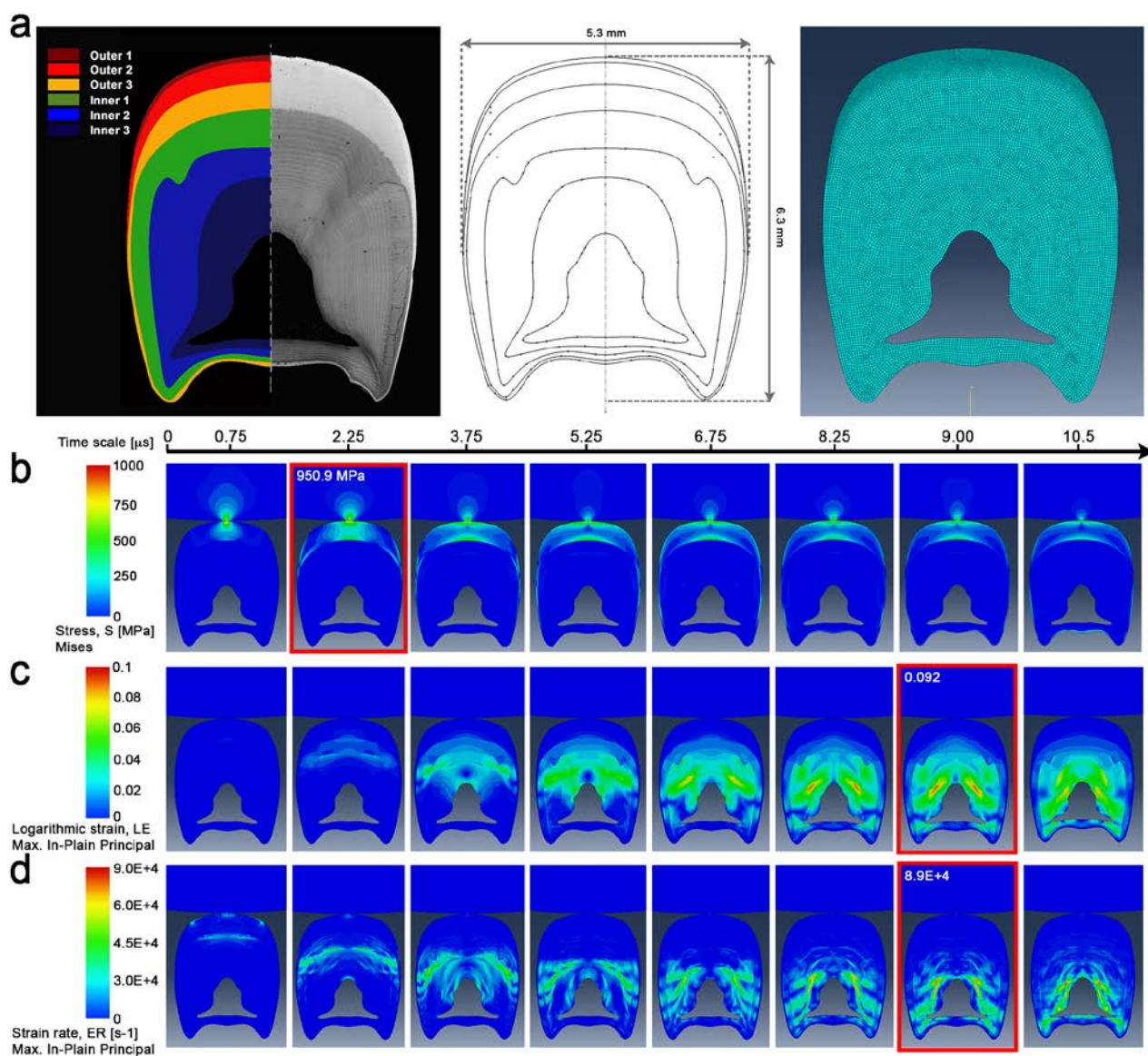
Supplementary Figure 4. Indentation stress-strain curves of geological fluorapatite (FAP), the spearer club outer layer, and the smasher club outer layer in both dry and hydrated conditions computed from partial loading-unloading indentation curves. While there is no difference for FAP between dry and hydrated conditions, the yield strength (σ_y) in the outer layer of the spearer and smasher clubs decrease by 0.2 GPa and 0.9 GPa, respectively. This decrease is likely related to the presence of organic components in these layers, which is higher in the smasher sample.



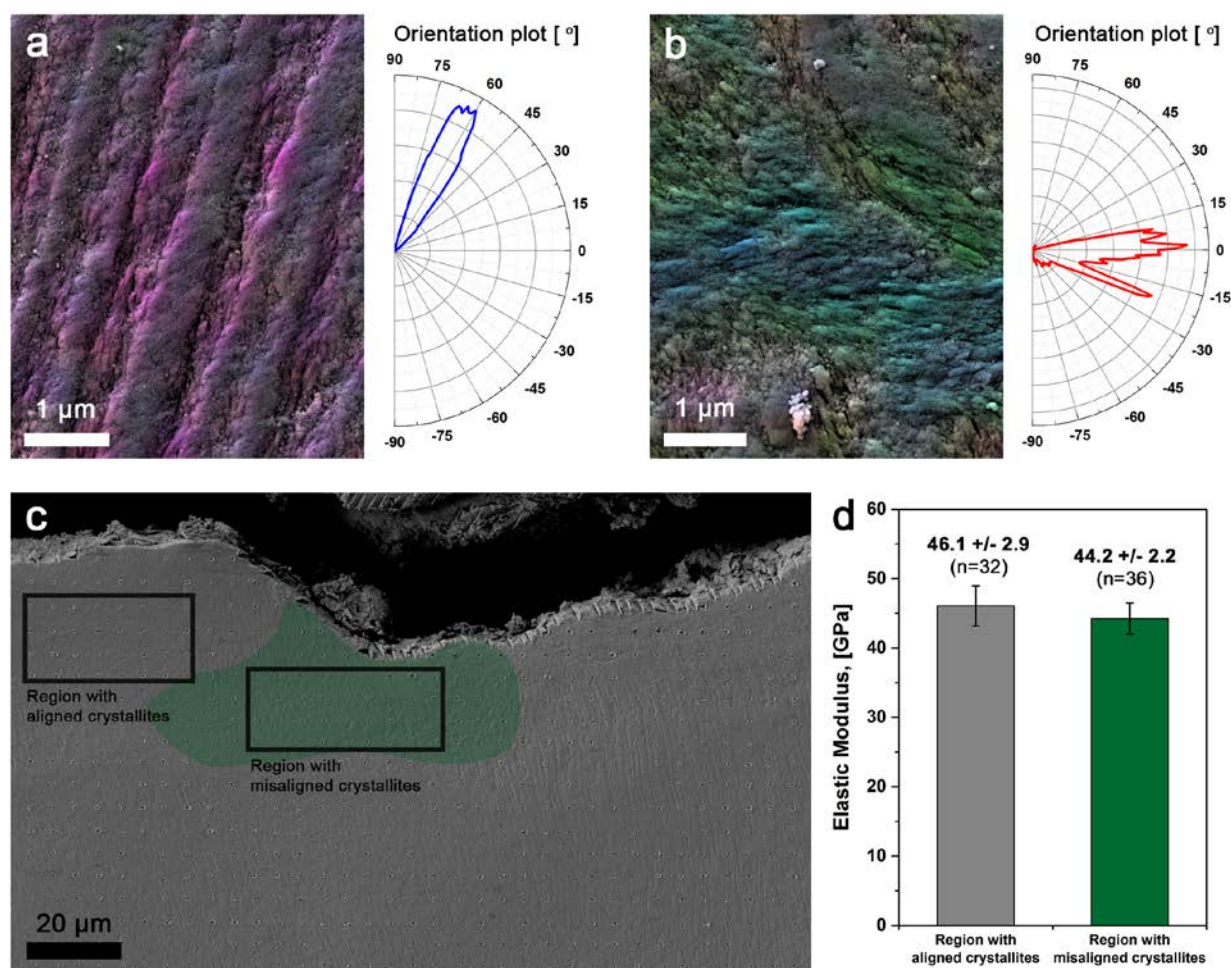
Supplementary Figure 5. Residual displacement after partial loading-unloading cycles in the inner layers of the dactyl clubs in hydrated conditions. Three cycles are highlighted (#11, #22, and #32) to emphasize the large residual displacements (h_r) upon unloading, which indicate that strain-hardening is due to a plastic deformation mechanism consisting of micro-channel densification (see main text).



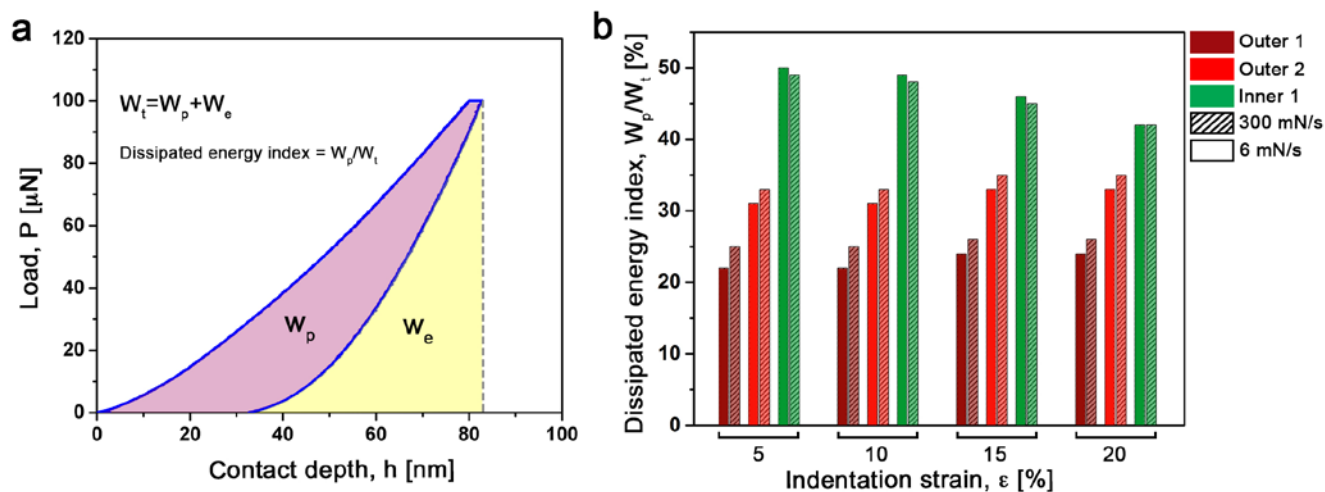
Supplementary Figure 6. Influence of the loading rate on the Hertzian indentation response. (a) Partial loading-unloading curves. **(b)** Computed indentation stress-strain curves in various layers. Loading rates ranged from 6 mN/s to 300 mN/s.



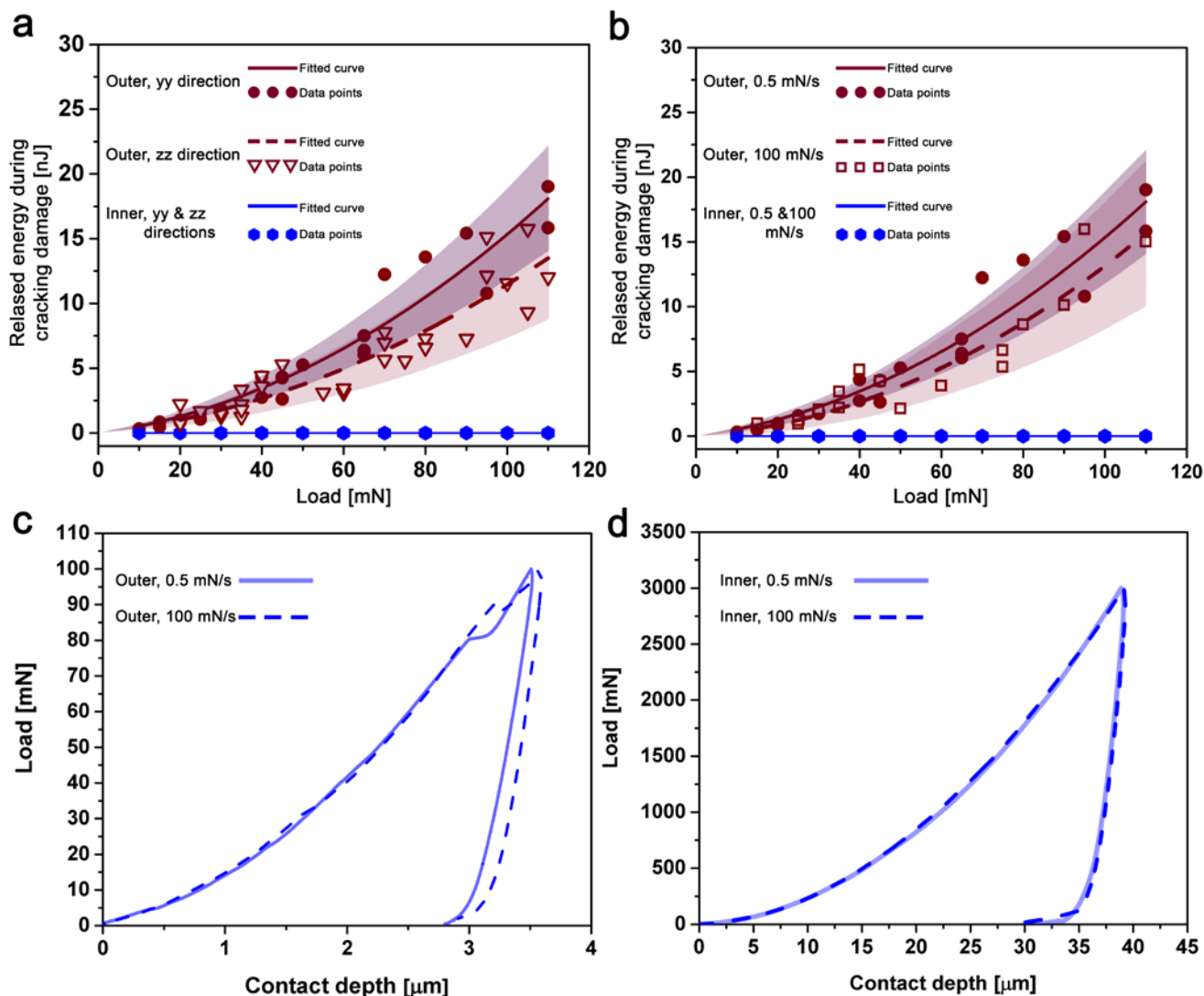
Supplementary Figure 7. Dynamic Finite Element Analysis of an impact against a stiff target (steel, $E = 200$ GPa). **(a)** Geometry of the club used for the simulation as obtained from FESEM images. The club was divided into six layers with constitutive relationships obtained by fitting the experimental indentation stress-strain curves shown in Figure 2 (main text). **(b)** Von Mises stress distribution showing that the maximum stress is reached 2.25 μ s after impact (frame highlighted in red). **(c)** Maximum strain and **(d)** maximum strain rate, which are reached in the innermost layers 9 μ s after impact (frames highlighted in red). Details of the computations are given in Supplementary Note 2.



Supplementary Figure 8. Quantitative analysis of crystallite orientation under a native contact and influence of crystallite rotation on the elastic modulus. (a, b) Distribution of crystallite orientation in the same locations as shown in Figure 3c of the main text, obtained using Image J for both (a) the oriented and (b) the misaligned regions. Color coding represents specific orientation, which is also represented on the orientation plots. **(c, d)** Average elastic moduli after native impact on regions with preferentially oriented crystallites (left) and misaligned crystallites (right).



Supplementary Figure 9. Energy absorption by plastic yielding during a Hertzian contact cycle. **(a)** Definition of the elastic energy (W_e), the plastic energy (W_p), and total contact energy (W_t). **(b)** (W_p/W_t) vs. indentation strain during a contact cycle in various layers and for two loading rates.



Supplementary Figure 10. Influence of the anisotropy and loading rate during sharp tip indentation. (a) Released cracking energy vs. indentation load in the yy and zz directions, illustrating a slightly higher absorption by plastic dissipation in the zz direction (lower cracking energy released). **(b)** Released energy vs. indentation load at low and high loading rates, showing no statistical differences between the two rates. Representative indentation curves on the outer **(c)** and inner **(d)** layers at low and high loading rates. In both regions, the loading rate had no significant influence on the sharp contact indentation response.

Supplementary Notes

Supplementary note 1: Tip calibration and stress-strain derivation

To calibrate the 10 μm cono-spherical tip, a wide range of forces (50 μN to 12,000 μN , total of 125 indents) were applied to standard polycarbonate and fused quartz samples, allowing to cover 35 to 1,700 nm of contact depth range. Using the extracted stiffness (S) values and known Young's moduli E of polycarbonate and fused quartz, the contact radii a were calculated from:

$$a = \frac{S}{2E}$$

a - h_c values were subsequently plotted and fitted with the following expression:

$$a = 13.879 \times (h_c + 68.00775)^{0.78572}$$

The tip radius R at each contact depth can then be calculated as:

$$\frac{a}{R} = \frac{1}{\sqrt{(\tan^{-2} \theta + 1)}}$$

where $a = f(h_c)$ is the contact radius, and ϑ is the tangent angle.

The indentation stress-strain points for each cycle was finally calculated using:

$$\varepsilon = \frac{a}{R}$$

$$\sigma = P_m = \frac{P}{\pi a^2}$$

Supplementary note 2: Dynamic finite element analysis (DFEA)

To simulate the impact event between the dactyl club and a rigid target, a 2D Planar model of the club and target was designed and analyzed using the commercial finite element software Abaqus/Explicit 6.15 under plane-strain conditions. The geometrical shape and dimensions of the club were acquired from FESEM micrographs, with the dimensions in the range 5 to 6 mm as shown in Supplementary Figure 7a. The club model consisted of six regions, as defined from the indentation experiments. The interfaces between the layers were assumed to be perfectly bonded through tie interface condition. A hemi-spherical stainless steel barrier ($E = 200$ GPa, density = $8,000 \text{ kg/m}^3$) of radius 10 mm was selected as a target. The contact between the club and target was defined as frictionless (tangential) and hard (normal). The club and steel target were discretized using plane-strain elements with reduced integration elements. After conducting mesh sensitivity analysis, three different mesh sizes of $1 \text{ }\mu\text{m}$, $10 \text{ }\mu\text{m}$ and $50 \text{ }\mu\text{m}$ were chosen for the outermost, the outer and the inner layers, and the target respectively. The finite element mesh contained a total of 23,615 nodes and 23,285 elements. The hollow-section in the club inner region was modeled as a stress-free with boundary.

The constitutive laws for each region was obtained by fitting the experimental Hertzian stress-strain curves in hydrated conditions. For the outer layers with the experimentally obtained elastic-plastic behavior, J2 plasticity with isotropic hardening behavior was used. For the inner layers, a strain stiffening hyper-elastic behavior (Ogden constitutive model with $n = 3$) was employed. Simulations were carried through finite strain by including non-linear geometry option in the software. The hemi-spherical steel target was fully constrained and a 20 m/s velocity was applied to the club along the normal direction. A total impact time of $30 \text{ }\mu\text{s}$ was imposed, consisting of both the impact and the retraction movement. Upon impact compressive waves travels in both the deformable target and club. Von-Mises effective stress, longitudinal logarithmic strain, and strain-rates were monitored. It is to be noted that the properties across the club are not uniformly graded, rather there are step changes in the properties from the outer stiff and strong inorganic mineral layer to inner organic rich layer. The banded stress contours in Supplementary Fig. 7b in the club are due to very different Young's moduli in the outer layers and inner layers. The maximum effective stress of 951 MPa was obtained in the outer layers of the club beneath the contact point at $2.25 \text{ }\mu\text{s}$.